



**HAL**  
open science

# Vertical Flux of Trace Elements Associated With Lithogenic and Biogenic Carrier Phases in the Southern Ocean

Stéphane Blain, H. Planquette, I. Obernosterer, A. Guéneuguès

► **To cite this version:**

Stéphane Blain, H. Planquette, I. Obernosterer, A. Guéneuguès. Vertical Flux of Trace Elements Associated With Lithogenic and Biogenic Carrier Phases in the Southern Ocean. *Global Biogeochemical Cycles*, 2022, 36 (5), 10.1029/2022GB007371 . hal-03684981

**HAL Id: hal-03684981**

**<https://hal.science/hal-03684981>**

Submitted on 1 Jun 2022

**HAL** is a multi-disciplinary open access archive for the deposit and dissemination of scientific research documents, whether they are published or not. The documents may come from teaching and research institutions in France or abroad, or from public or private research centers.

L'archive ouverte pluridisciplinaire **HAL**, est destinée au dépôt et à la diffusion de documents scientifiques de niveau recherche, publiés ou non, émanant des établissements d'enseignement et de recherche français ou étrangers, des laboratoires publics ou privés.

1 **Vertical flux of trace elements associated with lithogenic and biogenic carrier**  
2 **phases in the Southern Ocean**

3 **S. Blain<sup>1</sup>, H. Planquette<sup>2</sup>, I. Obernosterer<sup>1</sup>, A. Guéneuguès<sup>1</sup>**

4

5 <sup>1</sup> Sorbonne Université, CNRS, Laboratoire d'océanographie microbienne (LOMIC), 1 avenue  
6 Pierre Fabre, 66650 Banyuls sur mer, France.

7 <sup>2</sup> CNRS, IRD, Ifremer, LEMAR, University of Brest, Plouzané, France.

8

9 Corresponding author: Stéphane Blain (stephane.blain@obs-banyuls.fr)

10

11 **Key Points:**

- 12 • Export fluxes of 15 trace elements reveal contrasted seasonal patterns between  
13 lithogenic and biological carriers.
- 14 • Basalt particles are the major lithogenic carrier phase of 9 trace elements.
- 15 • Fecal pellets, diatom vegetative cells and spores are each carriers of distinct trace  
16 elements.

17

18 **Abstract**

19 Trace elements (TE) are tracers of multiple biotic and abiotic processes in the ocean and some  
20 of them are essential for marine life. Vertical export by particles is a major removal process of  
21 a large fraction of TE from the surface ocean. However, the seasonal export dynamics and its  
22 controlling factors, critical for the understanding of the internal TE cycling, remain poorly  
23 constrained. Here, we report and discuss the seasonal export of 15 TE in sinking particles  
24 collected by a sediment trap deployed in a highly productive region of the Southern Ocean.  
25 Basalt material was the main carrier phase for the export flux of 9 TE, and its dynamic was  
26 characterised by a strong decrease over time. TE export driven by biological carriers such as  
27 diatom spores and vegetative cells added pulsed seasonal dynamics to the lithogenic signal,  
28 while the contribution of fecal pellets was less variable over the season. For each TE, we were  
29 able to decipher the biological carrier phases that represent the most dominant export  
30 pathway. We discuss this partitioning with regards to the known metabolic functions of the  
31 different trace metals or TE of biological interest.

32

33

34  
35

## **1 Introduction**

36 During the past decade the international project GEOTRACES has undertaken an  
37 unprecedented effort to improve our knowledge of the distribution and biogeochemical cycles  
38 of trace elements and their isotopes (TEI) in the ocean (Anderson 2020). Trace metals are  
39 required in many metabolic functions (Sunda 2012) and as such, biogenic particles that are  
40 generated in the upper ocean are one of the main players regulating the internal cycling of so  
41 called “bioactive” trace elements (TE). TE are incorporated into particles through biological  
42 uptake and/or passive adsorption; they can then be remineralized, desorbed and/or ultimately  
43 exported. Particle sinking is one of the mechanisms of downward transport of chemical  
44 elements (Boyd et al. 2019). Large biogenic particles such as phytoplankton aggregates or  
45 fecal pellets are major vectors in the downward transport of particulate organic carbon (POC),  
46 but lithogenic particles can also play a role by ballasting aggregates and reducing  
47 remineralisation (Lemaitre et al. 2020). Due to their role in the control of atmospheric CO<sub>2</sub>  
48 (Antia et al. 2001), carbon vertical export fluxes have been extensively studied, yet TE export  
49 fluxes have been considerably less investigated.

50 Vertical fluxes of particulate TE can be determined in different ways (McDonnell et al. 2015).  
51 Among them, moored sediment traps have been used since the 1970s to measure vertical  
52 fluxes of sinking material in the ocean. Important characteristics of vertical fluxes were  
53 revealed by this approach, but possible biases and limitations were also identified leading to  
54 the delivery of best practises (Buesseler et al. 2007). Taking these recommendations into  
55 account for deployment of the moorings and their design, moored sediment traps are powerful  
56 tools and are quite unique to capture long term variability (months to years) of sinking fluxes  
57 including TEs (Kremling and Streu 1993; Huang and Conte 2009; Kuss et al. 2010; Conte et  
58 al. 2019). In the northern Sargasso Sea, the oceanic flux program (OFP) provides the longest  
59 time series for elemental composition of export fluxes at three depths. Data collected between

60 2000 and 2015 were used to build mean seasonal cycles for 19 elements with a monthly  
61 temporal resolution (Conte et al. 2019). Based on the assumption that the elemental  
62 composition of the upper continental crust approximated lithogenic material composition in  
63 the traps, elemental fluxes were partitioned between different phases (organic matter,  
64 carbonates, lithogenic, authigenic). Two components have been identified as main drivers of  
65 the seasonal dynamics of the elemental fluxes. One of them was coupled to the seasonal cycle  
66 of primary production and surface export. The other one was related to internal processes  
67 associated with chemical scavenging and particle aggregation (Conte et al. 2019).

68 Based on a 13 year time series of elemental flux composition at 2000 m in the North East  
69 Atlantic, the mean annual cycles (monthly resolution) of 13 elements were reported (Pullwer  
70 and Waniek 2020). Overall, depending on the element considered, weak or no seasonality was  
71 detected. This was likely due to a small biological signal at the seasonal level, which was  
72 further damped by interannual variability of environmental conditions in surface waters. The  
73 depth of the traps also likely contributed to mask a clear seasonal signal at this site.

74 In the Southern Ocean, moored sediment traps were also widely used to investigate carbon  
75 export dynamics (Honjo et al. 2000). However, studies of the seasonal dynamics of TE export  
76 are rare. The seasonality of particulate export fluxes of 8 TE was studied in the polynya of  
77 Pridz Bay (Sun et al. 2016). Seasonal variations of Cu, Zn and Cd were mainly driven by ice  
78 coverage and biological production whereas fluxes of Al, Fe and Mn mainly derived from  
79 continental debris were controlled by ice melting and freezing processes.

80 Further investigations of the seasonal export dynamics of TE, with high temporal resolution  
81 are therefore required. We have addressed this challenge in the Kerguelen Plateau, a  
82 productive region of the Southern Ocean, where iron fertilisation leads to a marked seasonal  
83 pattern of carbon export (Rembauville et al. 2015a; Blain et al. 2020). In this context, we  
84 aimed to study and understand the various processes impacting the stoichiometry and the

85 magnitude of these export fluxes, including the seasonal dynamics that can facilitate the  
86 partitioning of TE export between different carrier phases.

87

## 88 **2 Material and methods**

### 89 **2.1 Sediment trap and sensors.**

90 The sediment trap mooring was deployed during the SOCLIM cruise  
91 (doi/10.17600/16003300) on October 13<sup>th</sup> 2016, at a station located on the central Kerguelen  
92 plateau (50°38'344 °S, 71°59'854 °E) (Figure 1A) in the core of a productive region which is  
93 naturally iron fertilized (Blain et al. 2007). The bottom depth is 527 m. Two consecutive  
94 diatom blooms occur annually (Blain et al. 2020) with peaks in chlorophyll concentrations  
95 within the mixed layer in November and in December (Figure 1B).

96 We used a Technicap PPS3 sediment trap (0.125 m<sup>2</sup> collecting area, 4.75 aspect ratio) located  
97 at 292 m below the surface. The cups were prepared using trace metal clean protocols in a  
98 clean room. The cups were washed with warm solution alkaline detergent (Extran) for 24  
99 hours, rinsed 3 times with distilled water, then soaked in 2M HCl (analytical grade) for one  
100 week, rinsed 3 times with MQ water, soaked in 0.2 M HCl (ultrapure) for 1 week and finally  
101 rinsed 3 times with MQ water. The cups were then stored in plastic bags until used. Following  
102 the protocol of the preparation of the trace metal clean AQUIL medium (Price et al. 1989), the  
103 hypersaline formalin solution buffered at pH=8 with sodium tetraborate was passed through a  
104 Chelex resin to remove trace metal contamination. Trace metal concentrations of this solution  
105 can be found in Table S2. Just prior to the deployment, the 12 cups (250mL) were filled with  
106 the 5% preservative solution and mounted on the sediment trap carousel. The collection time  
107 for each cup was 11 days (Table 1). A current meter (Aquadopp) and an inclinometer were  
108 attached to the sediment trap to record measurements of current speeds and inclination of the  
109 trap at a frequency of 1 h<sup>-1</sup>.

110 After recovering the sediment traps on April 3<sup>rd</sup> 2017, 1 mL of the supernatant of the cups  
111 was immediately replaced by fresh hypersaline formalin buffered (pH=8) solution before  
112 storage at room temperature until further processing. Four months later, at the home  
113 laboratory, samples were first transferred to a Petri dish and examined under a  
114 stereomicroscope (Leica MZ8, x10 to x50 magnification) to remove swimmers (i.e. organisms  
115 for which the structure was well preserved and that actively entered the cup). Then the  
116 samples were split into eight aliquots using a Jencons peristaltic splitter (Rembauville et al.  
117 2015a).

118

## 119 **2.2 Bulk chemical analysis.**

120 Aliquots for chemical analyses were centrifuged for 5 min at 3000 rpm. After this step, the  
121 supernatant was withdrawn and replaced by Milli-Q-grade water to remove salts.

122 This rinsing step was repeated three times. The remaining pellet was freeze-dried (SGD-  
123 SERAIL, 0.05–0.1 mbar, -30 to 30°C, 48 h run) and weighed three times (Sartorius MC  
124 210 P balance, precision of 10<sup>-4</sup> g) to calculate the total mass. The particulate material was  
125 then ground to a fine powder and used for further elemental analysis.

126

### 127 **2.2.1 Mass, total POC/PON, BSi, CaCO<sub>3</sub>.**

128 For particulate organic carbon (POC) and particulate organic nitrogen (PON) analyses, 3 to 5  
129 mg of the freeze-dried powder was weighed directly into pre-combusted (450°C, 24 h) silver  
130 cups. Samples were decarbonated by adding 20 µL of 2M analytical-grade HCl (Sigma-  
131 Aldrich). Samples were dried overnight at 50°C. POC and PON were measured with a CHN  
132 analyser (Perkin Elmer 2400 Series II CHNS/O elemental analyser) calibrated with glycine.  
133 Samples were analysed in triplicate with an analytical precision of less than 0.7 %.

134 For BSi analysis, 2 to 8 mg of material was used. For BSi sample digestion we followed the  
135 protocol from (Ragueneau et al. 2005) and the silicic acid concentrations in the solutions were  
136 determined manually following Aminot and K erouel (2007). The precision of BSi  
137 measurement was 10% (Ragueneau et al. 2005).

138 For bulk CaCO<sub>3</sub> analyses, 5 mg of freeze-dried material was weighed into Teflon vials for the  
139 mineralization. One mL of 65% (v/v) HNO<sub>3</sub> (Sigma analytical grade) was added and samples  
140 were placed in an ultrasonication bath for 20min. Samples were then dried overnight at 130  
141  C, then 0.5 mL of 40% (v/v) HF (Sigma analytical grade) and 5 mL of 65% HNO<sub>3</sub> were  
142 added. The samples were ultra-sonicated a second time and dried overnight. The resulting  
143 residue was dissolved in 10 mL of 0.1N HNO<sub>3</sub> and the calcium (Ca) content was analyzed by  
144 inductively coupled plasma – optical emission spectrometry (ICP-OES, Perkin-  
145 ElmerOptima2000). The efficiency of the mineralization procedure was estimated using the  
146 reference material GBW-07314. The efficiency was 96% and the precision of the Ca  
147 measurement was 2% (Rembauville et al. 2016). Based on a Ca/Ti ratio in basalt of Kerguelen  
148 (3.3 mol/mol) we estimate that the contribution of Ca of lithogenic origin to the total Ca flux  
149 was low. We therefore equalled the Ca flux to the biological CaCO<sub>3</sub> flux.

150

### 151 **2.2.2 Elemental analysis by SF-ICP-MS**

152 For elemental analysis by SF-ICP-MS, between 12 and 40 mg of dried material were transferred  
153 into clean PFA vials and were digested in a mixture of 8.0M HNO<sub>3</sub> (Merck ultrapur) and 2.9M  
154 HF (Merck suprapur). Vials were tightly capped and heated to 130 C for 4 hours. The remaining  
155 solution was then evaporated to near dryness, then 400  L of concentrated HNO<sub>3</sub> (Merck  
156 ultrapur) was added to drive off the fluorides and was then evaporated. Finally, samples were  
157 redissolved with 3mL of 3% HNO<sub>3</sub> (Merck Ultrapur) and kept in acid-cleaned 15mL  
158 polypropylene tubes (Corning<sup> </sup>) until analysis by SF-ICP-MS (see details below). This

159 procedure has been proven adequate for digestion of all particulate trace metals (Planquette and  
160 Sherrell 2012).

161 All archive solutions were analyzed by SF-ICP-MS (Element XR) following the method of  
162 Planquette and Sherrell (2012). Final concentrations of samples and procedural blanks were  
163 calculated from In-normalized data. Analytical precision was assessed through replicate  
164 samples (every 10<sup>th</sup> sample) and accuracy was deduced from analysis of Certified Reference  
165 Materials (CRMs) of plankton (BCR-414) and sediments (PACS-3 and MESS-4)  
166 (Supplementary Table S1). Dissolved Mn, Fe, Cu, and Co concentrations of the saline solution  
167 were determined before deployment and after the recovery in an aliquot collected after the  
168 centrifugation, by SF-ICP-MS after preconcentration using the SeaFast (Supplementary Table  
169 S2) following the method described previously (Tonnard et al. 2020). Based on these results  
170 we calculated the percentage of dissolution of the particulate material within the cups  
171 (Supplementary Table S2). We did not correct particulate flux for dissolution as the values are  
172 generally low (<10%) with the exception of Mn (23.5%) in cup #11 and Cu in cups #7 (11.4  
173 %), #8 (10.1%) and #11 (30.8%).

174

### 175 **2.3 Carbon export fluxes of diatoms and faecal pellets.**

176 Microscopic observations were conducted within four months after recovery of the moorings.  
177 For the identification of diatoms, counting and size measurements, we followed the protocol  
178 described in Rembauville et al. (2015a) that allows the separate consideration of full and empty  
179 cells. For diatom counting, the samples were processed as follows. Two mL of one-eighth  
180 aliquot was diluted with 18 mL of artificial seawater and decanted in a Sedgewick Rafter  
181 counting chamber. Full diatoms were enumerated and identified under an inverted microscope  
182 with phase contrast (Olympus IX170) at 400x magnification. The morphometric measurements  
183 were done using high resolution images (Olympus DP71 camera) and Fiji image processing

184 software. The biovolume was calculated from morphometric measurements (Hillebrand et al.  
185 1999).

186 The export flux of diatoms ( $\text{Cell m}^{-2} \text{d}^{-1}$ ) was calculated using the equation:

$$187 \text{ Cell flux} = N_{\text{diat}} \times d \times 8 \times V_{\text{aliquot}} \times \frac{1}{0.125} \times \frac{1}{11} \times k \quad (\text{Eq. 1})$$

188 Where  $N_{\text{diat}}$  ( $\text{cell mL}^{-1}$ ) is the number of cells counted in one chamber,  $d$  is the dilution factor,  
189 8 relates to measurements being made on a one eighth aliquot of the sample,  $V_{\text{aliquot}}$  (mL) is the  
190 volume of the aliquot,  $1/0.125$  relates to the trap surface area (in  $\text{m}^2$ ),  $1/11$  relates to the sample  
191 collection time (in days), and  $k$  is the fraction of the chamber counted.

192 The diatom flux was then converted to POC flux for each taxon using allometric equations  
193 reported in the literature (Menden-Deuer and Lessard 2000; Cornet-Barthau et al. 2007) and  
194 taking into account specific relationships for spores (Rembauville et al. 2015a) (Table S3). The  
195 spore and vegetative cell carbon fluxes were then obtained by summing up the contribution of  
196 the different taxa. The sum of both fluxes corresponded to the carbon flux associated with  
197 diatoms.

198 To enumerate fecal pellets, an entire one-eighth aliquot of each sample cup was placed in a  
199 gridded Petri dish and observed under a stereomicroscope (Zeiss Discovery V20) coupled to a  
200 camera (Zeiss Axiocam ERc5s) at 10X magnification. Fecal pellets were classified into three  
201 types according to their shape: spherical, cylindrical, ovoid/ellipsoid (Table S3) (Gleiber et al.  
202 2012). Size measurements were used to calculate the volume of each fecal pellet according to  
203 their shape that was then converted to carbon using a factor of  $0.036 \text{ mg C mm}^{-3}$  (González and  
204 Smetacek 1994). The fecal pellets carbon fluxes ( $F_{\text{fp}}$  ( $\text{mg C m}^{-2} \text{d}^{-1}$ )) in the different size classes  
205 were calculated using the equation:

$$206 F_{\text{fp}} = C_{\text{fp}} \times 8 \times \frac{1}{0.125} \times \frac{1}{11} \quad (\text{Eq. 2})$$

207 where  $C_{\text{fp}}$  (mg C per fecal pellets for each type) is the concentration of carbon in each fecal  
208 pellet type. Others terms in the equation have the same definition as in Eq. 1). The  $F_{\text{fp}}$  were

209 finally summed to provide the total fecal carbon fluxes. Although the calculation of total POC  
210 flux is associated with large uncertainties (around 50%, (Rembauville et al. 2015a), the linear  
211 regression between  $POC_{\text{calculated}}$  and  $POC_{\text{measured}}$  was as follows:

$$212 \quad POC_{\text{calculated}} = (0.84 \pm 0.05) \times POC_{\text{measured}} + (0.2 \pm 0.35) \text{ with } R^2 = 0.9621$$

213

## 214 **2.4 Statistics tools and data visualisation.**

215 Statistical analysis (cross-correlation, Principal Component Analysis (PCA) and Partial least  
216 Square Regression (PLSR)) were performed using scikit-learn packages python 2.7. Scipy.stats  
217 package python 2.7 was used to conduct ANOVA after checking for homoscedasticity with a  
218 levene test. Data visualisation was realised with python 2.7 matplotlib library.

219

## 220 **3 Results**

### 221 **3.1 Physical conditions at the depth of the sediment trap**

222 The average depth of the sediment trap was  $293 \pm 2$  m ( $n=3152$ ) with a few short and episodic  
223 deepening events below 300 m (Fig. 2A). The mean inclination angle of the sediment trap was  
224  $0.8^\circ \pm 1^\circ$  (Fig. 2B). Inclination angles above  $2^\circ$  were rare and associated with deepening events  
225 of the trap and current speeds exceeding  $0.2 \text{ m s}^{-1}$ . The mean current speed was  $0.13 \pm 0.07 \text{ m}$   
226  $\text{s}^{-1}$ . The short-term variability of current speed and direction (Fig. 2C and 2D) was driven by  
227 tide (see Rembauville et al. 2015a) for a detailed study at the same site and depth) and a window  
228 of 26 h is adequate for filtering this short-term variability.

229

### 230 **3.2 Seasonal changes of mass flux and biological export.**

231 The seasonal variations of export fluxes were determined for particle mass, total POC and PON,  
232 for  $\text{CaCO}_3$  and BSi. POC was further partitioned between different biological carrier phases:  
233 total diatoms ( $POC_{\text{diat}}$ ), separated into diatom spores ( $POC_{\text{spore}}$ ) and diatom vegetative cells

234 (POC<sub>veg</sub>), and fecal pellets (POC<sub>fp</sub>)(Fig. 3). Seasonal variations of particle mass, POC, POC<sub>diat</sub>,  
235 and BSi fluxes were characterised by two peaks of export. The first export event occurred  
236 between 12 Nov 2016 and 15 Dec 2016 and was recorded in cups #3 to #5. A second export  
237 event occurred between 17 Jan 2017 and 08 Feb 2017 and was recorded in cups #9 and #10.  
238 The export of POC<sub>spore</sub> took place largely during the first event, while POC<sub>veg</sub> and CaCO<sub>3</sub>  
239 exports were mainly observed during the second event. High export fluxes of POC<sub>fp</sub> were also  
240 observed during these two main events (cups #4, #5 and #9). On a seasonal basis, the POC  
241 export was largely dominated by fecal pellets (89 %) while the relative contribution of diatoms  
242 (vegetative cells and spores) to total POC never exceeded 11%.

243

244 To better understand the seasonal variability of the export *via* different biological carrier phases  
245 we used principal component analysis (PCA) (Fig. 4). The first two principal components (PC)  
246 explained respectively 72.1 % and 20.8 % of the total variance. The first PC separated the cups  
247 in two categories. Positive values of PC1 correspond to cups with material collected during  
248 both major export events (#3, #4, #5 and #9, #10), and negative values of PC1 were related to  
249 the other cups. The highly correlated variables (mass, BSi, POC, PON, POC<sub>fp</sub>, POC<sub>diat</sub> and  
250 POC<sub>spore</sub>) (Figure S1) mainly contribute to PC1. The second component (PC2) separated mainly  
251 the first (negative values, #3, #4, #5) from the second export event (positive values, #9, #10).  
252 The variables contributing mainly to PC2 are POC<sub>spore</sub> associated with the first export event and  
253 POC<sub>veg</sub> and CaCO<sub>3</sub> associated with the second export event.

254

### 255 **3.3 Seasonal changes of TE export**

256 The 12 TE fluxes varied by almost 7 orders of magnitude (Figure 5). The highest flux was  
257 recorded for Al with a maximum of 160  $\mu\text{mol m}^{-2} \text{d}^{-1}$  and the lowest for Th with a minimum of  
258  $3.5 \times 10^{-2} \text{ nmol m}^{-2} \text{d}^{-1}$ . Examination of the seasonal changes revealed two qualitatively different

259 temporal patterns. High export fluxes of P, Cd, Ba, Mo, Cu, Ni and V were associated with one  
260 or both of the main export events described in the previous section. For most of these elements,  
261 the export fluxes were higher during the first than during the second event, but more subtle  
262 differences appear. For example, the flux of Cd export was much more pronounced during the  
263 first than the second event, whereas for V the fluxes were almost identical during both events.  
264 For the other elements (Y, Mn, Zr, Co, Ti, Cr, Th, Fe and Al) the highest fluxes were measured  
265 in the first cups (#1 to #5) and the lowest in the remaining cups (#6 to #12).

266

267 For TE fluxes, a PCA confirms the partitioning between the two main groups mentioned in the  
268 previous section based on the qualitative analysis of the seasonal changes (Figure 6). The two  
269 first components of the PCA explain 98.2 % of the seasonal variation of the TE export. For  
270 PC1, positive scores correspond to the beginning of the season (#1 to #5) and negative scores  
271 to the remaining cups (#6 to #12). The highest positive scores for the PC2 are typical of cups  
272 corresponding to the two export events (#4 #5 and #9 #10). Within the group of elements  
273 characterised by two marked peaks of export (P, Cd, Ba, Mo, Cu, Ni and V), the PCA shows  
274 three possible subgroups where seasonal variations of these elements are highly correlated.  
275 These consist of P, Cd and Ba, then Mo and Cu, and finally Ni and V (Figure S2).

276

#### 277 **4 Discussion**

278 Our parallel observations of the seasonal changes in the export fluxes of different biological  
279 carrier phases, as defined hereafter, and of trace metals, provide the opportunity to identify the  
280 the main factors that control their export in this iron fertilized region of the Southern Ocean.

281 The bulk composition of particles is usually partitioned between different pools identified as  
282 particulate organic matter (POM), biogenic silica (BSi), calcium carbonate (CaCO<sub>3</sub>), lithogenic  
283 and authigenic material (Lam et al. 2015). The partitioning of TEs between these different pools

284 relies on two main hypotheses. First, one assumes that it is possible to identify a chemical  
285 element or a chemical form of the element that largely dominates one of the pools and has a  
286 minor contribution to the others. For the lithogenic fraction, Al has been extensively used,  
287 although Ti has recently gained interest in this context when the potential source material and  
288 its chemical composition are clearly identified. For the POM fraction, beside POC that is widely  
289 used, phosphorus (P) is also selected as the reference element, because it is a major contributor  
290 and has a mineral form (e.g. apathite) with low abundance in seawater. In addition, P is  
291 measured simultaneously with metals by analytical methods like Sector Field Induced Coupled  
292 Plasma Mass Spectrometry (SF-ICP-MS) or X-ray Fluorescence (XRF) synchrotron (Twining  
293 et al. 2003).

294

295 The second assumption is that for any given element, the ratio with the reference element of a  
296 given fraction must be known or postulated. For the lithogenic pool, the elemental composition  
297 of a representative material can be used in order to determine enrichment factors. These  
298 enrichment factors provide information on the extent to which TE are associated with particles  
299 of lithogenic origin. In most studies, global crustal composition or upper crustal compositions  
300 (Taylor and McLennan 1995) are used, but the composition of local mineral sources like desert  
301 dust are also valuable (Kremling and Streu 1993). For the biogenic fractions,  $\text{CaCO}_3$  and BSi  
302 determinations are straightforward, but there are few experimental data to constrain the ratio of  
303 a given TE to  $\text{CaCO}_3$  ( $\text{TE}/\text{CaCO}_3$ ) and BSi ( $\text{TE}/\text{BSi}$ ) and therefore to derive directly the amount  
304 of metal transported by these fractions. The issue is even more complicated for POM due to the  
305 diverse composition of this fraction. When POM is dominated by phytoplankton, an extension  
306 of the Redfield ratio to metals can be considered, but there are large uncertainties in the  
307 determination of phytoplankton TE/P ratios (Twining and Baines 2013). Moreover, elemental  
308 ratios of dead microorganisms can largely differ from those measured in living cells due to the

309 dissolution and remineralization rates that vary between elements. Consequently, TE/P ratios  
310 in two important vectors of TE export, phytoplankton aggregates (Twining et al. 2015) or fecal  
311 pellets (Fowler 1977) cannot easily be inferred. For example, different types of particulate  
312 organic matter (Lam et al. 2015) could influence surface adsorption of TEs (Balistrieri et al.  
313 1981) and ultimately the TE stoichiometry. Together, these considerations result in a complex  
314 dynamic of TEs hosted in dissolved and particulate pools. This is further complicated by the  
315 fact that the magnitude of external sources and individual processes are subjected to strong  
316 variations throughout the year (Sternberg et al. 2007; Hayes et al. 2015).

317

318 In the following, we will discuss our findings from several points of view. First, we will use an  
319 approach classically found in the literature and summarised above that provides an estimate of  
320 the lithogenic contribution to the TE flux. This approach allows the derivation of the flux not  
321 supported by lithogenic carriers which can approximate the biological, scavenged, and  
322 authigenic contributions. Secondly, we will consider simultaneously several possible carrier  
323 phases to extract the ones most probably associated with the individual elements. This second  
324 approach will be used to investigate further the role of different biological carriers. We will  
325 confront these results with recent findings on the biological role of TE in both autotrophic and  
326 heterotrophic microorganisms, as revealed by laboratory or in situ omics-based studies.

327

#### 328 **4.1 Basalt is the main lithogenic carrier phase.**

329 Using the results of the PCA for TE (Figure 6), we show that Y, Mn, Cr, Ti, Co, Th, Fe, Al and  
330 Zr have a similar seasonal export pattern. Some of these elements are well known as  
331 representatives of lithogenic matter (i.e. Ti, Cr, Zr, Y, Th and Al), while others like Mn, Co and  
332 Fe are also involved in biological processes. The quantitative estimate of the lithogenic fraction  
333 of the fluxes relies on both the choice of a reference element and a reference material of a known

334 elemental composition. Al and Ti have been both used previously as reference elements. In the  
335 present study we will not use Al because it is known to be associated with diatom frustules (Ren  
336 et al. 2013) and a previous study above the Kerguelen plateau has shown that diatoms dominate  
337 during spring and summer (Blain et al. 2020). Therefore, Al is likely present in diatoms  
338 exported directly via aggregates or indirectly via fecal pellets. Using Al as the reference could  
339 therefore lead to an overestimation of the lithogenic fraction, while Ti can provide a more  
340 conservative estimate. We thus consider Ti as a reference element for the lithogenic fraction  
341 (Ohnemus and Lam 2014) and calculated the mass ratios  $F_{TE}/F_{Ti}$  where  $F_{TE}$  is the export flux of  
342 a given TE and  $F_{Ti}$  is the export flux of Ti collected in the same cup (Table 2).

343  
344 The choice of the elemental ratio is also critical for the calculation of the lithogenic contribution  
345 to TE export fluxes. In the present study, for most of the elements associated mainly with a  
346 lithogenic carrier phase, Al, Fe, Cr, Co, Y, Zr, (Figure 6) the TE/Ti ratios (Table 2) are not  
347 significantly different ( $p=0.01$ ) from the composition of basalt rocks collected around the  
348 Kerguelen plateau and islands (Kerguelen archipelago, Heard and Mac Donald Islands) (Weis  
349 et al. 1993; Yang et al. 1998). However, with the exception of Cr and Y, the TE/Ti ratios  
350 measured in the sediment trap differed largely from that typical of upper continental crust  
351 (UCC) (Taylor and McLennan 1995) (Table 2). Yet, the large differences for Fe/Ti and Al/Ti  
352 ratios resulted very likely from the high Ti content of island basalt (Prytulak and Elliott 2007).  
353 We also note that the Mn/Ti ratios are not significantly different from Kerguelen basalt, if a few  
354 basalt samples with low Ti (ratio<2) are excluded from this analysis. Therefore, derived basalt  
355 particles are likely the main contributors to the lithogenic export fluxes, although alteration of  
356 rocks and subsequent transformation during transport in terrestrial and marine environments  
357 could modify the chemical composition of lithogenic particles.

358

359 We calculated for individual elements the average TE/Ti based on: i) all cups and ii) only the  
360 first two cups and compared with the TE/Ti ratios in the UCC and in the Kerguelen basalt  
361 (Table 2). We then estimated the lithogenic contribution to TE export fluxes using equation 3:

$$362 \quad F_{TE_{lith}} = (TE/Ti) \times F_{Ti} \text{ (Eq. 3),}$$

363 where TE/Ti is the average ratio for the two first cups. In Figure 4, the projection of cups #1  
364 and #2 presented the most negative score along PC1 suggesting that TE export fluxes collected  
365 in this trap were mainly driven by non-biological carriers. Moreover, the PCA of TE export  
366 fluxes (Figure 6) shows that the projections of cups#1 and #2 were located in the quarter of  
367 space that was related to a suite of TEs typically associated with basalt. This analysis of both  
368 PCAs clearly identify these cups as mainly associated with lithogenic material and suggests  
369 they are therefore the most appropriate to estimate a lithogenic elemental ratio for the sediment  
370 trap material. We note that including cups #3, #4 and #5 in the calculation of the individual  
371 elemental ratio would have resulted in a biased estimate due to the contribution of biological  
372 fluxes. We also calculated the residual export flux, which is not associated with lithogenic  
373 material for each element using equation 4:

$$374 \quad F_{xs} = F_{TE} - F_{TE_{lith}} \text{ (Eq. 4)}$$

375 and these residual fluxes are represented on Figure 7.

376 Our observations clearly underscore that the residual export fluxes of 6 elements (Zr, Co, Cr,  
377 Th, Fe, Al) estimated using this ratio are occasionally or consistently negative throughout the  
378 season (Figure 7). Regarding Fe, the order of magnitude of an expected biogenic flux based on  
379 the export flux of P ( $P_{xs}$ ) can be estimated. Considering the highest values of  $P_{xs}$  of  $50 \mu\text{mol}$   
380  $\text{m}^{-2} \text{d}^{-1}$  in cup#5, and using a high estimate for the Fe quota ( $\text{Fe:P}=5 \text{ mmol mol}^{-1}$  (Twining and  
381 Baines 2013)), one would expect  $0.25 \mu\text{mol m}^{-2} \text{d}^{-1}$  of biogenic Fe at the time of the peak flux.  
382 This represents around 0.5 % of the total flux of Fe measured (Figure 5), confirming that such

383 low contributions cannot be detected using the calculation of the residual fluxes ( $F_{xs}$  Eq. 4).  
384 This result, together with the negative values of residual export fluxes, highlight that any  
385 contribution of a carrier phase (e.g. biological) other than basalt derived particles cannot be  
386 detected using this approach.

387

#### 388 **4.2 Role of different biological carriers in the export of TE.**

389 In the following, we consider the 9 elements (P, Cd, Ba, Mo, Cu, Ni, V, Y, Mn) for which  $F_{xs}$   
390 are positive throughout the season (Figure 7). Among these, 7 elements (P, Mo, Cd, Cu, Ni, V,  
391 Mn) have known biological functions and can therefore be directly associated with biological  
392 carrier phases. Overall, this is confirmed by the seasonal dynamics of their  $F_{xs}$  that presented 1  
393 or 2 maxima corresponding to the cups that collected sinking material during the first (cups# 3,  
394 4, 5) or second (cups# 9, 10) export event. To go a step forward, we took advantage of the  
395 detailed description of biological matter export provided by microscopic observations  
396 (Rembauville et al. 2015a) in the same cup material. An important aspect was to quantify the  
397 carbon content of exported diatoms and all types of fecal pellets. Microscopic observations  
398 revealed that diatoms dominated the phytoplankton community (Blain et al. 2020), and that 12  
399 different taxa contributed significantly (>1% of total biomass) to both the surface carbon  
400 biomass and carbon export. However, the concentrations of TE with a biological role certainly  
401 varied throughout the season in surface waters due to intense uptake and remineralisation as  
402 observed for Fe above the Kerguelen plateau (Blain et al. 2008; Bowie et al. 2015). Similarly,  
403 TE quota are likely to vary over time in surface diatoms, with consequences on TE composition  
404 of the fecal pellets. The absence of data on seasonal changes in TE concentrations in the water  
405 column and the large uncertainty of the TE transfer efficiency between phytoplankton and  
406 zooplankton led us to make a rather conservative choice of only three biological carriers,

407 vegetative cells, spores and fecal pellets. Additionally, we considered the total particle mass,  
408 POC, PON, POC<sub>diat</sub>, and used CaCO<sub>3</sub> as a tracer of calcifying organisms.

409

410 We first investigated the role of these different biological carriers using PCA (Figure S3) based  
411 on  $F_{xs}$  and the different biological carriers mentioned above. However, this approach did not  
412 prove informative on the association of a given TE with a biological carrier, except for V, which  
413 was strongly associated with vegetative cells and/or calcifying organisms exported during the  
414 second bloom. The strong association of Mn with the first bloom, as revealed by the PCA, is  
415 not meaningful, because  $F_{xs}$  of Mn is high only in cup #3 albeit the export of this bloom is  
416 collected by cups #4 and #5 as well (Blain et al. 2020). For Ba and Y, the PCA does not provide  
417 any clues on their association with a particular biological carrier. Co-linearity between the  
418 different biological descriptors may have hampered the emergence of more significant  
419 relationships for other elements.

420

421 We have therefore analysed the data set using a different statistical tool, the Partial Least Square  
422 Regression (PLSR), also referred to as Projection of Latent Structure Regression (Abdi 2010).  
423 This method considers a set of predictors (X) and descriptors (Y) and extracts a single set of  
424 scores from both simultaneously. The method can be seen as a simultaneous PCA on X and Y  
425 which achieves the best relationships between X and Y. The method is efficient even when the  
426 variables are possibly correlated and when the number of variables is large compared to the  
427 number of observations. This method has been successfully applied to determine the ecological  
428 vectors associated with sinking carbon flux (Rembauville et al. 2015), to predict the partitioning  
429 of carbon within plankton assemblages based on bio-optical properties (Rembauville et al.  
430 2017) or to link biological diversity and carbon fluxes (Guidi et al. 2016). To apply PLSR we  
431 considered the total export flux of the 15 elements (descriptors) and the different biological

432 vectors (predictors) mentioned above, and we considered Ti as an overall predictor of lithogenic  
433 material. It is important to note that with this approach the search for relationships between  
434 elements and the lithogenic carrier phase does not require the use of an elemental ratio. To  
435 summarize the results of the PLSR analysis we present the projections of both descriptors and  
436 predictors in a three-dimensional space defined by the three first latent variables (Figure 8)  
437 which represent 57.5%, 22.1% and 8.6 % of the covariance, respectively. The three  
438 corresponding 2D dimensional projections in the latent vectors space are provided in Figure S4.  
439 Three different groups of TE emerge from this analysis.

440

441 **TEs associated with the lithogenic carrier phase.** The PLSR, clearly identifies a group of  
442 TEs (Al, Zr, Cr, Fe, Th, Co, Mn and Y) for which the seasonal dynamics are strongly related to  
443 the lithogenic carrier phase, represented by Ti. This result is in line with the conclusions of the  
444 PCA and TE<sub>xs</sub> analysis (Figure 6).

445

446 **TEs associated with fecal pellets and diatom spores.** The export of Cd, P and Ba was strongly  
447 associated with POC<sub>fp</sub> and to a lesser extend to POC<sub>sp</sub>. For Ba, this result is not surprising  
448 considering that particulate Ba is largely found as authigenic mineral barite in the ocean  
449 (Dehairs et al. 1980), formed by precipitation from dissolved Ba in microenvironments where  
450 it becomes supersaturated with respect to barite. Such environments are fecal pellets (Alldredge  
451 and Cohen 1987; Ploug 2001) or aggregates like marine snow which in our study contained  
452 large quantities of spores (Blain et al. 2020). Strong correlations of Cd and P export fluxes have  
453 already been observed with sediment traps deployed in the upper water column (> 1500m)  
454 whereas this relationship vanished at greater depth (Ho et al. 2011; Conte et al. 2019). In the  
455 present study, the export of Cd was mainly driven by spores during the first bloom and by fecal  
456 pellets throughout the season, while vegetative cells and calcifying organisms present during

457 the second bloom played a minor role for Cd export. Cd, but also Co, can substitute for Zn in  
458 the carbonic anhydrase (CA) enzyme, Cd-CA and Zn-CA, respectively (Morel et al. 2020).  
459 This has been demonstrated for diatoms under low Zn conditions (Lane and Morel 2000). Cd-  
460 CA is present in *Thalassiosira antarctica*, *Chaetoceros dichatea*, *Proboscia alata* and  
461 *Proboscia inermis* (Morel et al. 2020), species that were well represented in our sediment traps  
462 (Blain et al. 2020). Interestingly *T. antarctica* and *C. dichatea* are small and spore forming  
463 diatoms which dominated during the first bloom, while the genus *Proboscia* contains large  
464 diatoms exported as vegetative cells that thrived during the second bloom. Cd utilisation by  
465 different diatoms in surface waters could explain the seasonal variation of Cd export in the  
466 sediment traps. Cd can also be coincidentally taken up by the divalent transporter under Fe-  
467 limited conditions (Lane et al. 2008; Horner et al. 2013). At the beginning of the season, the  
468 reservoir of Zn and Fe was large above the Kerguelen plateau (Wang et al. 2019), but the rapid  
469 development of the massive bloom of small diatoms could lead to a rapid decrease in Zn to  
470 levels at which the substitution of Zn by Cd in CA occurred and/or Cd being taken up by the  
471 divalent transporter. No strong signal of particulate Cd was associated with the second bloom  
472 suggesting that the substitution of Zn by Cd in CA or divalent transport uptake are not dominant  
473 processes at the end of the productive season, either due to increased Zn or Fe concentrations  
474 provided by remineralisation after the first bloom or due to lower requirements of large diatom  
475 cells which do not need Cd for CA activities. Although calcifying organisms including  
476 coccolithophorids, present during the second bloom, have high Cd requirements (Ho et al. 2003;  
477 Sunda 2012), their contribution was likely hidden behind the large fluxes associated with fecal  
478 pellets.

479

480 **TEs associated with lithogenic and biological carrier phases.** V, Mo, Cu and Ni export fluxes  
481 are both driven by lithogenic and biological carrier phases. This is a consequence of both their

482 significant contribution to Kerguelen basalt composition (Table 2) and their biological role in  
483 microorganisms. Using a similar approach to that used for Cd, we examine the seasonal  
484 dynamics of the export of these four metals by first summarizing a few recent insights on their  
485 biological role for microorganisms relevant for our study. We then discuss how these  
486 observations can provide clues to understand the seasonal dynamics of their export.

487 The main non-lithogenic V export event coincided with the flux of large vegetative diatoms and  
488 calcifying organisms after the second bloom (Figure 6). Due to the similar seasonal patterns of  
489 these biological carrier phases, it is not possible, based on PLSR, to make a clear preferential  
490 association with either of them. The current knowledge on the biological role of V is mainly  
491 related to diatoms, thus our discussion on the temporal changes of V export focuses on this  
492 phytoplankton group. V is a cofactor of haloperoxidase enzymes (VHPO) that produce organo-  
493 halogens (Moore et al. 1996; Murphy et al. 2000; Hill and Manley 2009). Haloperoxidase  
494 activity by diatoms could alter the quorum sensing of prokaryotes and therefore protect diatoms  
495 against algicidal prokaryotes (Amin et al. 2012). In contrast to the seasonal dynamics of all  
496 other elements, the export of V associated to the biological fraction was higher during the  
497 second than during the first bloom (Figure 7). Seasonal observations of diatom and prokaryotic  
498 communities in the surface layer revealed compositional changes and strong associations  
499 (positive and negative) between diatom species and prokaryotic taxa (Liu et al. 2020). Positive  
500 associations could result from interactions based on the exchange of metabolites between  
501 diatoms and prokaryotes for resource acquisition, but negative associations are more difficult  
502 to interpret. The seasonal dynamics of non-lithogenic particulate V, if related to VHPO activity,  
503 could suggest that some diatoms efficiently reduce the growth of targeted prokaryotic taxa with  
504 algicidal activity in the phycosphere.

505

506 The prevalence of non-lithogenic particulate V during the second bloom could be related to  
507 seasonal changes of the bioavailability of Fe. Haloperoxidase can contain Fe-heme as prosthetic  
508 group instead of V. Fe-heme containing enzymes could dominate the haloperoxidase activity  
509 of diatoms when the bioavailable Fe stock is high such as at the beginning of the season.  
510 However, as biological uptake during the first bloom consumed a large part of the bioavailable  
511 Fe, haloperoxidase activity of diatoms dominating during the second bloom may have switched  
512 to VHPO, which requires the uptake of vanadate, an anion that is always present at non-limiting  
513 concentrations in seawater. V can also be found in nitrogenase (*nif*) involved in the fixation of  
514 dinitrogen (N<sub>2</sub>) where it substitutes Mo. A recent study illustrated that Mo/Fe containing *nif*  
515 genes are overexpressed by prokaryotic communities on marine particles (Debeljak et al. 2021).  
516 Therefore, the association of V or Mo with vegetative diatoms could partly be explained by N<sub>2</sub>  
517 fixing prokaryotes attached to particles and their downward transport could be a biological  
518 carrier phase for Mo and V.

519

520 The dominant biological carrier phase for Cu was different to that of V and Mo. Cu export was  
521 mainly related to diatom spores and to a lesser extend to fecal pellets whereas no clear  
522 association with vegetative cells and CaCO<sub>3</sub> was observed (Figure 8 and Figure S4). Cu is a co-  
523 factor of a large number of oxidative enzymes involved in different metabolic pathways  
524 including Fe acquisition (Maldonado and Price 2001) and nitrogen cycling (Kuypers et al.  
525 2018). Another noticeable feature of these Cu proteins is that most of them are located outside  
526 eukaryotic cells or in the periplasm of prokaryotes (Silva and Williams 2001). A possible  
527 consequence can be that Cu enzymes are prone to rapid degradation and release of Cu following  
528 cell death. Fecal pellets or spores could provide a protected environment during export, which  
529 could explain our observations.

530

531 The biological carrier phases for Ni were mainly diatoms (spores or vegetative cells) and fecal  
532 pellets had a minor role. Among the many biological pathways, Ni is involved in the  
533 assimilation of urea (Oliveira and Antia 1984) and is also the cofactor of an enzyme of the  
534 superoxide dismutase (SOD) family which can substitute for Fe-superoxide dismutase in low  
535 Fe environments (Dupont et al. 2010; Cuvelier et al. 2010). These requirements for Ni likely  
536 lead to high Ni quota of diatoms relative to other phytoplankton groups (Twining et al. 2012).  
537 It was, however, also noted that 50% of Ni contained in diatoms is associated with the frustule  
538 with an unknown function. These Ni dependent enzymes suggest that diatom spores, vegetative  
539 cells and fecal pellets that contained mainly diatoms are all potential biological vectors of Ni  
540 export. If true, the lack of a marked difference between the first and the second bloom  
541 dominated by spores and vegetative cells, respectively, is surprising. A larger contribution of  
542 diatoms to Ni export would be expected during the second bloom for two reasons. First, the  
543 assimilation of urea is likely only noticeable when the switch from  $\text{NO}_3^-$  to  $\text{NH}_4^+$  uptake has  
544 occurred, thus after the first bloom. Second, since Fe bioavailability was lower during the  
545 second bloom, Fe-SOD is likely to be replaced by Ni-SOD. We suggest an additional process  
546 to significantly contribute to the biological export of Ni. Methanogenic *Archaea* utilise different  
547 enzymes belonging to the hydrogenase, reductase or CO dehydrogenase families where Ni is  
548 present as co-factor (Mulrooney and Hausinger 2003). Methanogenic *Archaea* have been  
549 detected in different marine particles like marine snow or fecal pellets (Maarel et al. 1999)  
550 where they could thrive within anoxic niches (Alldredge and Cohen 1987; Ploug 2001). A time  
551 series of the composition of the particulate matter in the surface layers would certainly provide  
552 new data required to decipher between these different hypotheses.

553

## 554 **5 Conclusion**

555 Our observations of the seasonal particulate TE export in a productive region of the Southern  
556 Ocean have revealed that the identification of the carrier phases is critical for our understanding  
557 of the export dynamics of individual TE. The lithogenic and biological carrier phases identified  
558 in our study had distinct temporal patterns. Basalt particles, the main lithogenic carrier phase  
559 dominated the export flux early in the season and strongly decreased over time, reflected in the  
560 particulate export pattern of TE representative of lithogenic matter (Ti, Cr, Zr, Y, Th and Al)  
561 and of TE with a defined biological role (Mn, Co and Fe). The biological carrier phases, diatom  
562 vegetative cells and spores, revealed two pulsed export events, while vertical transport *via* fecal  
563 pellets remained stable over time. TE with known biological functions (Cd, Ba, Mo, Cu, Ni and  
564 V) were associated with one or both of these main export events.

565 A further look into the seasonal variability of stocks of bioavailable TE is necessary to better  
566 understand how these influence the phytoplankton assemblage, inherent enzyme strategies, and  
567 subsequent TE utilisation and exports. Finally, future studies should investigate TE composition  
568 of individual fecal pellets produced by different zooplankton species feeding on distinct food  
569 sources. This could provide insight to help decipher the contribution of each zooplankton  
570 species to TE export.

571

## 572 **Acknowledgments, Samples, and Data**

573 We thank the captains and the crew of the R/V Marion Dufresne for their support during the  
574 two cruises. We thank E. de Saint Léger, F. Pérault from DT-INSU, and people of IPEV (Institut  
575 Polaire Paul Emile Victor) for the technical support during preparation, deployment and  
576 recovery of moorings. We thank Nathalie Leblond (Laboratoire Océanographie de Villefranche  
577 sur mer) for processing the samples and performing chemical analysis. We thank Mathieu  
578 Rembauville for his help during deployment of the clean traps. We thank the anonymous  
579 reviewers and the associated editor for their careful reading of the manuscript and for their

580 comments and suggestions that have improved of our manuscript. This work is part of the  
581 project SOCLIM supported by the Climate Initiative of the foundation BNP Paribas, the French  
582 research program LEFE-CYBER of INSU-CNRS, IPEV, Sorbonne Université, and the Flotte  
583 Océanographique Française. This work was also supported by the project SEATRAK funded  
584 by the French research program LEFE-CYBER. The authors declare no conflict of interest.  
585 Data are available at the SEANOE database <https://www.seanoe.org/data/00606/71768/>

586

587

588 **References**

589

590 Abdi, H. 2010. Partial least squares regression and projection on latent structure regression (PLS  
591 Regression). *WIREs Comp Stat* **2**: 97–106. doi:10.1002/wics.51

592 Alldredge, A. L., and Y. Cohen. 1987. Can Microscale Chemical Patches Persist in the Sea?

593 Microelectrode Study of Marine Snow, Fecal Pellets. *Science* **235**: 689–691.

594 doi:10.1126/science.235.4789.689

595 Amin, S. A., M. S. Parker, and E. V. Armbrust. 2012. Interactions between Diatoms and Bacteria.

596 *Microbiology and Molecular Biology Reviews* **76**: 667–684. doi:10.1128/MMBR.00007-12

597 Aminot, A., and R. K erouel. 2007. Dosage automatique des nutriments dans les eaux marines :

598 m ethodes en flux continu, Ifremer.

599 Anderson, R. F. 2020. GEOTRACES: Accelerating Research on the Marine Biogeochemical Cycles of

600 Trace Elements and Their Isotopes. *Annu. Rev. Mar. Sci.* **12**: 49–85. doi:10.1146/annurev-

601 marine-010318-095123

602 Antia, A. N., W. Koeve, G. Fischer, and others. 2001. Basin-wide particulate carbon flux in the Atlantic

603 Ocean: Regional export patterns and potential for atmospheric CO<sub>2</sub> sequestration. *Global*

604 *Biogeochem. Cycles* **15**: 845–862. doi:10.1029/2000GB001376

605 Balistrieri, L., P. G. Brewer, and J. W. Murray. 1981. Scavenging residence times of trace metals and

606 surface chemistry of sinking particles in the deep ocean. *Deep Sea Research Part A.*

607 *Oceanographic Research Papers* **28**: 101–121. doi:10.1016/0198-0149(81)90085-6

608 Blain, S., B. Qu eguiner, L. Armand, and others. 2007. Effect of natural iron fertilisation on carbon

609 sequestration in the Southern Ocean. *Nature* **446**: 1070–1075. doi:doi:10.1038/nature05700

610 Blain, S., M. Rembauville, O. Crispi, and I. Obernosterer. 2020. Synchronized autonomous sampling

611 reveals coupled pulses of biomass and export of morphologically different diatoms in the

612 Southern Ocean. *Limnol Oceanogr* Ino.11638. doi:10.1002/lno.11638

613 Blain, S., G. Sarthou, and P. Laan. 2008. Distribution of dissolved iron during the natural iron-  
614 fertilization experiment KEOPS (Kerguelen Plateau, Southern Ocean). *Deep Sea Research Part*  
615 *II: Topical Studies in Oceanography* **55**: 594.

616 Bowie, A. R., P. van der Merwe, F. Qu  rou  , and others. 2015. Iron budgets for three distinct  
617 biogeochemical sites around the Kerguelen Archipelago (Southern Ocean) during the natural  
618 fertilisation study, KEOPS-2. *Biogeosciences* **12**: 4421–4445. doi:10.5194/bg-12-4421-2015

619 Boyd, P. W., H. Claustre, M. Levy, D. A. Siegel, and T. Weber. 2019. Multi-faceted particle pumps  
620 drive carbon sequestration in the ocean. *Nature* **568**: 327–335. doi:10.1038/s41586-019-  
621 1098-2

622 Buesseler, K. O., A. N. Antia, M. Chen, and others. 2007. An assessment of the use of sediment traps  
623 for estimating upper ocean particle fluxes. *J. Mar. Res.* **65**: 345–416.  
624 doi:10.1357/002224007781567621

625 Conte, M. H., A. M. Carter, D. A. Koweeck, S. Huang, and J. C. Weber. 2019. The elemental  
626 composition of the deep particle flux in the Sargasso Sea. *Chemical Geology* **511**: 279–313.  
627 doi:10.1016/j.chemgeo.2018.11.001

628 Cornet-Barthau, V., L. Armand, and B. Qu  guiner. 2007. Biovolume and biomass estimates of key  
629 diatoms in the Southern Ocean. *Aquatic Microbial Ecology* **48**: 295–308.

630 Cuvelier, M. L., A. E. Allen, A. Monier, and others. 2010. Targeted metagenomics and ecology of  
631 globally important uncultured eukaryotic phytoplankton. *Proceedings of the National*  
632 *Academy of Sciences* **107**: 14679–14684. doi:10.1073/pnas.1001665107

633 Debeljak, P., S. Blain, A. Bowie, P. Merwe, B. Bayer, and I. Obernosterer. 2021. Homeostasis drives  
634 intense microbial trace metal processing on marine particles. *Limnol Oceanogr* **66**: 3842–  
635 3855. doi:10.1002/lno.11923

636 Dehairs, F., R. Chesselet, and J. Jedwab. 1980. Discrete suspended particles of barite and the barium  
637 cycle in the open ocean. *Earth and Planetary Science Letters* **49**: 528–550. doi:10.1016/0012-  
638 821X(80)90094-1

639 Dupont, C. L., K. N. Buck, B. Palenik, and K. Barbeau. 2010. Nickel utilization in phytoplankton  
640 assemblages from contrasting oceanic regimes. *Deep Sea Research Part I: Oceanographic*  
641 *Research Papers* **57**: 553–566. doi:10.1016/j.dsr.2009.12.014

642 Fowler, S. W. 1977. Trace elements in zooplankton particulate products. *Nature* **269**: 51–53.  
643 doi:10.1038/269051a0

644 Gleiber, M., D. Steinberg, and H. Ducklow. 2012. Time series of vertical flux of zooplankton fecal  
645 pellets on the continental shelf of the western Antarctic Peninsula. *Mar. Ecol. Prog. Ser.* **471**:  
646 23–36. doi:10.3354/meps10021

647 González, H., and V. Smetacek. 1994. The possible role of the cyclopoid copepod *Oithona* in retarding  
648 vertical flux of zooplankton faecal material. *Mar. Ecol. Prog. Ser.* **113**: 233–246.  
649 doi:10.3354/meps113233

650 Guidi, L., S. Chaffron, L. Bittner, and others. 2016. Plankton networks driving carbon export in the  
651 oligotrophic ocean. *Nature* **532**: 465–470. doi:10.1038/nature16942

652 Hayes, C. T., J. N. Fitzsimmons, E. A. Boyle, D. McGee, R. F. Anderson, R. Weisend, and P. L. Morton.  
653 2015. Thorium isotopes tracing the iron cycle at the Hawaii Ocean Time-series Station  
654 ALOHA. *Geochimica et Cosmochimica Acta* **169**: 1–16. doi:10.1016/j.gca.2015.07.019

655 Hill, V. L., and S. L. Manley. 2009. Release of reactive bromine and iodine from diatoms and its  
656 possible role in halogen transfer in polar and tropical oceans. *Limnol. Oceanogr.* **54**: 812–822.  
657 doi:10.4319/lo.2009.54.3.0812

658 Hillebrand, H., C.-D. Dürselen, D. Kirschtel, U. Pollinger, and T. Zohary. 1999. Biovolume calculation  
659 for pelagic and benthic microalgae. *Journal of Phycology* **35**: 403–424. doi:10.1046/j.1529-  
660 8817.1999.3520403.x

661 Ho, T.-Y., W.-C. Chou, H.-L. Lin, and D. D. Sheu. 2011. Trace metal cycling in the deep water of the  
662 South China Sea: The composition, sources, and fluxes of sinking particles. *Limnol. Oceanogr.*  
663 **56**: 1225–1243. doi:10.4319/lo.2011.56.4.1225

664 Ho, T.-Y., A. Quigg, Z. V. Finkel, A. J. Milligan, K. Wyman, P. G. Falkowski, and F. M. M. Morel. 2003.  
665 The elemental composition of some marine phytoplankton. *Journal of Phycology* **39**: 1145–  
666 1159. doi:10.1111/j.0022-3646.2003.03-090.x

667 Honjo, S., R. Francois, S. Manganini, J. Dymond, and R. Collier. 2000. Particle fluxes to the interior of  
668 the Southern Ocean in the Western Pacific sector along 170[deg]W. *Deep Sea Research Part*  
669 *II: Topical Studies in Oceanography* **47**: 3521.

670 Horner, T. J., R. B. Y. Lee, G. M. Henderson, and R. E. M. Rickaby. 2013. Nonspecific uptake and  
671 homeostasis drive the oceanic cadmium cycle. *Proceedings of the National Academy of*  
672 *Sciences* **110**: 2500–2505. doi:10.1073/pnas.1213857110

673 Huang, S., and M. H. Conte. 2009. Source/process apportionment of major and trace elements in  
674 sinking particles in the Sargasso sea. *Geochimica et Cosmochimica Acta* **73**: 65–90.  
675 doi:10.1016/j.gca.2008.08.023

676 Kremling, K., and P. Streu. 1993. Saharan dust influenced trace element fluxes in deep North Atlantic  
677 subtropical waters. *Deep Sea Research Part I: Oceanographic Research Papers* **40**: 1155–  
678 1168. doi:10.1016/0967-0637(93)90131-L

679 Kuss, J., J. J. Waniek, K. Kremling, and D. E. Schulz-Bull. 2010. Seasonality of particle-associated trace  
680 element fluxes in the deep northeast Atlantic Ocean. *Deep Sea Research Part I:*  
681 *Oceanographic Research Papers* **57**: 785–796. doi:10.1016/j.dsr.2010.04.002

682 Kuypers, M. M. M., H. K. Marchant, and B. Kartal. 2018. The microbial nitrogen-cycling network. *Nat*  
683 *Rev Microbiol* **16**: 263–276. doi:10.1038/nrmicro.2018.9

684 Lam, P. J., D. C. Ohnemus, and M. E. Auro. 2015. Size-fractionated major particle composition and  
685 concentrations from the US GEOTRACES North Atlantic Zonal Transect. *Deep Sea Research*  
686 *Part II: Topical Studies in Oceanography* **116**: 303–320. doi:10.1016/j.dsr2.2014.11.020

687 Lane, E. S., K. Jang, J. T. Cullen, and M. T. Maldonado. 2008. The interaction between inorganic iron  
688 and cadmium uptake in the marine diatom *Thalassiosira oceanica*. *Limnol. Oceanogr.* **53**:  
689 1784–1789. doi:10.4319/lo.2008.53.5.1784

690 Lane, T. W., and F. M. M. Morel. 2000. A biological function for cadmium in marine diatoms.  
691 Proceedings of the National Academy of Sciences **97**: 4627–4631.  
692 doi:10.1073/pnas.090091397

693 Lemaitre, N., H. Planquette, F. Dehairs, and others. 2020. Particulate Trace Element Export in the  
694 North Atlantic (GEOTRACES GA01 Transect, GEOVIDE Cruise). ACS Earth Space Chem. **4**:  
695 2185–2204. doi:10.1021/acsearthspacechem.0c00045

696 Liu, Y., S. Blain, crispi, olivier, and I. Obernosterer. 2020. Seasonal dynamics of prokaryotes and their  
697 associations with diatoms in the Southern Ocean as revealed by an autonomous sampler.  
698 Environmental Microbiology. doi:10.1111/1462-2920.15184

699 Maarel, M. J. E. C., W. Sprenger, R. Haanstra, and L. J. Forney. 1999. Detection of methanogenic  
700 archaea in seawater particles and the digestive tract of a marine fish species. FEMS  
701 Microbiology Letters **173**: 189–194. doi:10.1111/j.1574-6968.1999.tb13501.x

702 Maldonado, M. T., and N. M. Price. 2001. Reduction and transport of organically bound iron by  
703 thalassiosira oceanica (bacillariophyceae). Journal of Phycology **37**: 298–310.  
704 doi:10.1046/j.1529-8817.2001.037002298.x

705 McDonnell, A. M. P., P. J. Lam, C. H. Lamborg, and others. 2015. The oceanographic toolbox for the  
706 collection of sinking and suspended marine particles. Progress in Oceanography **133**: 17–31.  
707 doi:10.1016/j.pocean.2015.01.007

708 Menden-Deuer, S., and E. J. Lessard. 2000. Carbon to volume relationships for dinoflagellates,  
709 diatoms, and other protist plankton. Limnol. Oceanogr. **45**: 569–579.  
710 doi:10.4319/lo.2000.45.3.0569

711 Moore, R. M., M. Webb, R. Tokarczyk, and R. Wever. 1996. Bromoperoxidase and iodoperoxidase  
712 enzymes and production of halogenated methanes in marine diatom cultures. J. Geophys.  
713 Res. **101**: 20899–20908. doi:10.1029/96JC01248

714 Morel, F. M. M., P. J. Lam, and M. A. Saito. 2020. Trace Metal Substitution in Marine Phytoplankton.  
715 *Annu. Rev. Earth Planet. Sci.* **48**: annurev-earth-053018-060108. doi:10.1146/annurev-earth-  
716 053018-060108

717 Mulrooney, S. B., and R. P. Hausinger. 2003. Nickel uptake and utilization by microorganisms. *FEMS*  
718 *Microbiol Rev* **27**: 239–261. doi:10.1016/S0168-6445(03)00042-1

719 Murphy, C. D., R. M. Moore, and R. L. White. 2000. Peroxidases from marine microalgae. *Journal of*  
720 *Applied Phycology* **12**: 507–513. doi:10.1023/A:1008154231462

721 Ohnemus, D. C., and P. J. Lam. 2014. Cycling of lithogenic marine particles in the US GEOTRACES  
722 North Atlantic transect. *Deep Sea Research Part II: Topical Studies in Oceanography*.  
723 doi:10.1016/j.dsr2.2014.11.019

724 Oliveira, L., and N. J. Antia. 1984. Evidence of nickel ion requirement for autotrophic growth of a  
725 marine diatom with urea serving as nitrogen source. *British Phycological Journal* **19**: 125–  
726 134. doi:10.1080/00071618400650131

727 Planquette, H., and R. M. Sherrell. 2012. Sampling for particulate trace element determination using  
728 water sampling bottles: methodology and comparison to in situ pumps. *Limnol. Oceanogr.*  
729 *Methods* **10**: 367–388. doi:10.4319/lom.2012.10.367

730 Ploug, H. 2001. Small-scale oxygen fluxes and remineralization in sinking aggregates. *Limnol.*  
731 *Oceanogr.* **46**: 1624–1631. doi:10.4319/lo.2001.46.7.1624

732 Price, N. M., G. I. Harrison, J. G. Hering, R. J. Hudson, P. M. Nirel, B. Palenik, and F. M. Morel. 1989.  
733 Preparation and chemistry of the artificial algal culture medium Aquil. *Biological*  
734 *Oceanography* **6**: 443–461.

735 Prytulak, J., and T. Elliott. 2007. TiO<sub>2</sub> enrichment in ocean island basalts. *Earth and Planetary Science*  
736 *Letters* **263**: 388–403. doi:10.1016/j.epsl.2007.09.015

737 Pullwer, J., and J. J. Waniek. 2020. Particulate trace metal fluxes in the center of an oceanic desert:  
738 Northeast Atlantic subtropical gyre. *Journal of Marine Systems* **212**: 103447.  
739 doi:10.1016/j.jmarsys.2020.103447

740 Ragueneau, O., N. Savoye, Y. Del Amo, J. Cotten, B. Tardiveau, and A. Leynaert. 2005. A new method  
741 for the measurement of biogenic silica in suspended matter of coastal waters: using Si:Al  
742 ratios to correct for the mineral interference. *Continental Shelf Research* **25**: 697–710.  
743 doi:10.1016/j.csr.2004.09.017

744 Rembauville, M., S. Blain, L. Armand, B. Quéguiner, and I. Salter. 2015a. Export fluxes in a naturally  
745 iron-fertilized area of the Southern Ocean – Part 2: Importance of diatom resting spores and  
746 faecal pellets for export. *Biogeosciences* **12**: 3171–3195. doi:10.5194/bg-12-3171-2015

747 Rembauville, M., N. Briggs, M. Ardyna, and others. 2017. Plankton Assemblage Estimated with BGC-  
748 Argo Floats in the Southern Ocean: Implications for Seasonal Successions and Particle Export:  
749 *Journal of Geophysical Research: Oceans* **122**: 8278–8292. doi:10.1002/2017JC013067

750 Rembauville, M., J. Meilland, P. Ziveri, R. Schiebel, S. Blain, and I. Salter. 2016. Planktic foraminifer  
751 and coccolith contribution to carbonate export fluxes over the central Kerguelen Plateau.  
752 *Deep Sea Research Part I: Oceanographic Research Papers* **111**: 91–101.  
753 doi:10.1016/j.dsr.2016.02.017

754 Rembauville, M., I. Salter, N. Leblond, A. Gueneugues, and S. Blain. 2015b. Export fluxes in a naturally  
755 iron-fertilized area of the Southern Ocean – Part 1: Seasonal dynamics of particulate organic  
756 carbon export from a moored sediment trap. *Biogeosciences* **12**: 3153–3170.  
757 doi:10.5194/bg-12-3153-2015

758 Ren, H., B. G. Brunelle, D. M. Sigman, and R. S. Robinson. 2013. Diagenetic aluminum uptake into  
759 diatom frustules and the preservation of diatom-bound organic nitrogen. *Marine Chemistry*  
760 **155**: 92–101. doi:10.1016/j.marchem.2013.05.016

761 Silva, J. J. R. F. da, and R. J. P. Williams. 2001. *The biological chemistry of the elements: the inorganic  
762 chemistry of life*, 2nd ed. Oxford University Press.

763 Sternberg, E., C. Jeandel, J.-C. Miquel, B. Gasser, M. Souhaut, R. Arraes-Mescoff, and R. Francois.  
764 2007. Particulate barium fluxes and export production in the northwestern Mediterranean.  
765 *Marine Chemistry* **105**: 281–295. doi:10.1016/j.marchem.2007.03.003

766 Sun, W.-P., Z.-B. Han, C.-Y. Hu, and J.-M. Pan. 2016. Source composition and seasonal variation of  
767 particulate trace element fluxes in Prydz Bay, East Antarctica. *Chemosphere* **147**: 318–327.  
768 doi:10.1016/j.chemosphere.2015.12.105

769 Sunda, W. G. 2012. Feedback Interactions between Trace Metal Nutrients and Phytoplankton in the  
770 Ocean. *Frontiers in Microbiology* **3**. doi:10.3389/fmicb.2012.00204

771 Taylor, S. R., and S. M. McLennan. 1995. The geochemical evolution of the continental crust. *Rev.*  
772 *Geophys.* **33**: 241. doi:10.1029/95RG00262

773 Tonnard, M., H. Planquette, A. R. Bowie, and others. 2020. Dissolved iron in the North Atlantic Ocean  
774 and Labrador Sea along the GEOVIDE section (GEOTRACES section GA01). *Biogeosciences* **17**:  
775 917–943. doi:10.5194/bg-17-917-2020

776 Twining, B. S., and S. B. Baines. 2013. The Trace Metal Composition of Marine Phytoplankton. *Annual*  
777 *Review of Marine Science* **5**: 191–215. doi:10.1146/annurev-marine-121211-172322

778 Twining, B. S., S. B. Baines, N. S. Fisher, J. Maser, S. Vogt, C. Jacobsen, A. Tovar-Sanchez, and S. A.  
779 Sañudo-Wilhelmy. 2003. Quantifying Trace Elements in Individual Aquatic Protist Cells with a  
780 Synchrotron X-ray Fluorescence Microprobe. *Anal. Chem.* **75**: 3806–3816.  
781 doi:10.1021/ac034227z

782 Twining, B. S., S. B. Baines, S. Vogt, and D. M. Nelson. 2012. Role of diatoms in nickel biogeochemistry  
783 in the ocean: DIATOMS AND NICKEL BIOGEOCHEMISTRY. *Global Biogeochem. Cycles* **26**: n/a-  
784 n/a. doi:10.1029/2011GB004233

785 Twining, B. S., S. Rauschenberg, P. L. Morton, and S. Vogt. 2015. Metal contents of phytoplankton  
786 and labile particulate material in the North Atlantic Ocean. *Progress in Oceanography* **137**:  
787 261–283. doi:10.1016/j.pocean.2015.07.001

788 Wang, R.-M., C. Archer, A. R. Bowie, and D. Vance. 2019. Zinc and nickel isotopes in seawater from  
789 the Indian Sector of the Southern Ocean: The impact of natural iron fertilization versus  
790 Southern Ocean hydrography and biogeochemistry. *Chemical Geology* **511**: 452–464.  
791 doi:10.1016/j.chemgeo.2018.09.010

792 Weis, D., F. A. Frey, H. Leyrit, and I. Gautier. 1993. Kerguelen Archipelago revisited: geochemical and  
793 isotopic study of the Southeast Province lavas. *Earth and Planetary Science Letters* **118**: 101–  
794 119. doi:10.1016/0012-821X(93)90162-3

795 Yang, H.-J., F. A. Frey, D. Weis, A. Giret, D. Pyle, and G. Michon. 1998. Petrogenesis of the Flood  
796 Basalts Forming the Northern Kerguelen Archipelago: Implications for the Kerguelen Plume.  
797 *Journal of Petrology* **39**: 711–748. doi:10.1093/etroj/39.4.711

798

799

**Table 1 : Sampling dates for sediment trap**

Cup number	Opening date	Closing date
1	20/10/2016	01/11/2016
2	01/11/2016	12/11/2016
3	12/11/2016	23/11/2016
4	23/11/2016	04/12/2016
5	04/12/2016	15/12/2016
6	15/12/2016	26/12/2016
7	26/12/2016	06/01/2017
8	06/01/2017	17/01/2017
9	17/01/2017	28/01/2017
10	28/01/2017	08/02/2017
11	08/02/2017	19/02/2017
12	19/02/2017	01/03/2017

Table 2 : **TE/Ti ratio**. In the first column, the star associated with a given trace element indicates that the mean TE/Ti in Kerguelen basalt and in sediment trap matter is not statistically different ( $p=0.01$ ).

<sup>(a)</sup> mean elemental ratios in continental crust (CC) from (Taylor and McLennan 1995). <sup>(b)</sup> Mean elemental ratios derived from composition of basalt rocks of Kerguelen island (Weis et al. 1993; Yang et al. 1998). <sup>(c)</sup> Mean elemental ratios considering all cups. <sup>(d)</sup> Ratio elemental ratios considering the two first cups.

TE	Upper CC <sup>(a)</sup>	Basalt <sup>(b)</sup>	cups#1-12 <sup>(c)</sup>	cups#1-2 <sup>(d)</sup>
	TE/Ti (g/g)	TE/Ti (g/g)	TE/Ti (g/g)	TE/Ti (g/g)
<b>Ti</b>	<b>1</b>	<b>1</b>	<b>1</b>	<b>1</b>
<b>Al*</b>	26.7	<b>4.2 ± 1.6</b>	<b>5.3 ± 0.7</b>	6.4
<b>Fe*</b>	11.7	<b>5.0 ± 1.7</b>	<b>4.2 ± 0.7</b>	4.4
Mn	0.2	(8.6 ± 2.4) 10 <sup>-2</sup>	(6.3 ± 0.8) 10 <sup>-2</sup>	5.2 10 <sup>-2</sup>
P	0.23	(2.5 ± 1.0) 10 <sup>-5</sup>	6.9 ± 4.9	0.68
Ba	0.18	(1.6 ± 0.9) 10 <sup>-3</sup>	0.9 ± 0.6	0.18
V	2 10 <sup>-2</sup>	(1.4 ± 0.3) 10 <sup>-2</sup>	(2.9 ± 1.8) 10 <sup>-2</sup>	1.1 10 <sup>-2</sup>
<b>Cr*</b>	1.2 10 <sup>-2</sup>	<b>(0.7 ± 1.4) 10<sup>-2</sup></b>	<b>(1.2 ± 0.2) 10<sup>-2</sup></b>	1.1 10 <sup>-2</sup>
<b>Co*</b>	3.3 10 <sup>-3</sup>	<b>(2.4 ± 1.2) 10<sup>-3</sup></b>	<b>(1.8 ± 0.2) 10<sup>-3</sup></b>	1.7 10 <sup>-3</sup>
Ni	6.6 10 <sup>-3</sup>	(4.9 ± 7.8) 10 <sup>-3</sup>	(2.7 ± 1.5) 10 <sup>-2</sup>	1.1 10 <sup>-2</sup>
<b>Y*</b>	7.3 10 <sup>-3</sup>	<b>(1.8 ± 0.6) 10<sup>-3</sup></b>	<b>(2.3 ± 0.6) 10<sup>-3</sup></b>	1.5 10 <sup>-3</sup>
<b>Zr*</b>	6.3 10 <sup>-2</sup>	<b>(1.4 ± 0.7) 10<sup>-2</sup></b>	<b>(6.9 ± 1.0) 10<sup>-2</sup></b>	6.8 10 <sup>-2</sup>
Th	3.5 10 <sup>-3</sup>	(1.7 ± 1.2) 10 <sup>-4</sup>	(5.8 ± 1.2) 10 <sup>-5</sup>	7.0 10 <sup>-4</sup>

800 **Figure captions:**

801

802 **Figure 1: Kerguelen plateau bloom.** a) Monthly composite of chlorophyll surface  
803 concentration ( $\text{mg m}^{-3}$ ) for November 2016. The white dot denotes the location of the sediment  
804 trap mooring. b) Seasonal variation of chlorophyll ( $\text{mg m}^{-3}$ ). The blue line corresponds to the  
805 8-day composite chlorophyll concentrations over the season of sediment trap deployment. The  
806 green line and light green area represent the climatology and standard deviation respectively.  
807 The white rectangles along the x axis denote the 12 periods of sediment trap collection.

808 **Figure 2: Physical environment of the sediment trap.** For all panels, the grey line shows the  
809 raw data acquired every 30 minutes. The black line denotes the running average with a time  
810 window of 26 hours. A) depth of the sediment trap, B) Inclination angle of the sediment trap  
811 (vertical reference =  $0^\circ$ ), C) current speed measured 3 m below the sediment trap. D) Current  
812 direction and intensity.

813 **Figure 3: Export fluxes of biological vectors.** Each panel shows the seasonal variations of the  
814 export flux of the parameter indicated in the upper left corner. Within each panel, vertical bars  
815 represent the export fluxes determined in the 12 cups.  $\text{POC}_{\text{diat}}$  is the flux associated with  
816 diatoms,  $\text{POC}_{\text{spore}}$  is the flux associated with diatom spores,  $\text{POC}_{\text{veg}}$  is flux associated with  
817 diatom vegetative cells and  $\text{POC}_{\text{fp}}$  is the flux associated with fecal pellets.

818 **Figure 4: PCA correlation biplots of biological fluxes.** Black dots denote the cups associated  
819 with their labels from 1 to 12 (1 corresponds to the first cup collected). Blue arrows represent  
820 the projection of the descriptors into the two first principal component plan (for clarity their  
821 lengths were multiplied by 2). The definition of arrow labels are  $C_{\text{tot}}$  (flux of total POC),  $N_{\text{tot}}$   
822 (flux of total PON),  $C_{\text{veg}}$  (flux of POC associated with vegetative diatoms),  $C_{\text{spore}}$  (flux of POC  
823 from diatom spores),  $C_{\text{fp}}$  (flux of POC from fecal pellets),  $\text{CaCO}_3$  (flux of  $\text{CaCO}_3$ ),  $m$  (flux of  
824 total particle mass) and  $\text{BSi}$  (flux of biogenic silica).

825 **Figure 5: Export fluxes of phosphorus and 11 trace elements.** Each individual panel shows  
826 the seasonal variability of the export flux of the element with its unit indicated in the left upper  
827 corner. Within each panel, vertical bars represent the export fluxes collected in the 12 cups and  
828 the vertical lines show the standard deviation based of analytical precision.

829 **Figure 6: PCA correlation biplots of trace elements:** Black dots denote the cups associated  
830 with their labels from 1 to 12 (1 corresponds to the first cup collected). Blue arrows represent  
831 the projection of the descriptors into the two first principal component plan (for clarity their  
832 lengths were multiplied by 2).

833 **Figure 7: Residual export of trace elements.** Each individual panel shows the seasonal  
834 variability of the residual export flux  $F_{xs}$  (see text for definition) of the element with its unit  
835 indicated in the left upper corner.

836 **Figure 8: Partitioning of total trace element export fluxes between different carrier**  
837 **phases.** The plot presents the projections of both predictors (in black) and descriptors (in blue)  
838 in a 3-dimensional space formed by the 3 first latent variables resulting from PLSR analysis  
839 which explained 57.5%, 22.1% and 8.6% of the covariance.

Figure 1

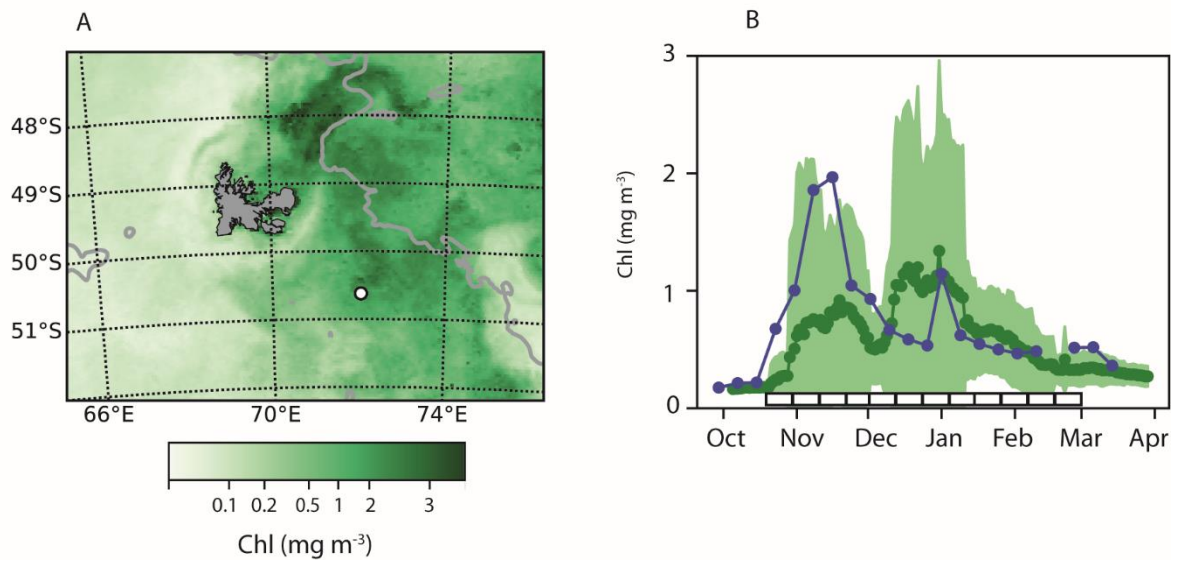


Figure 2

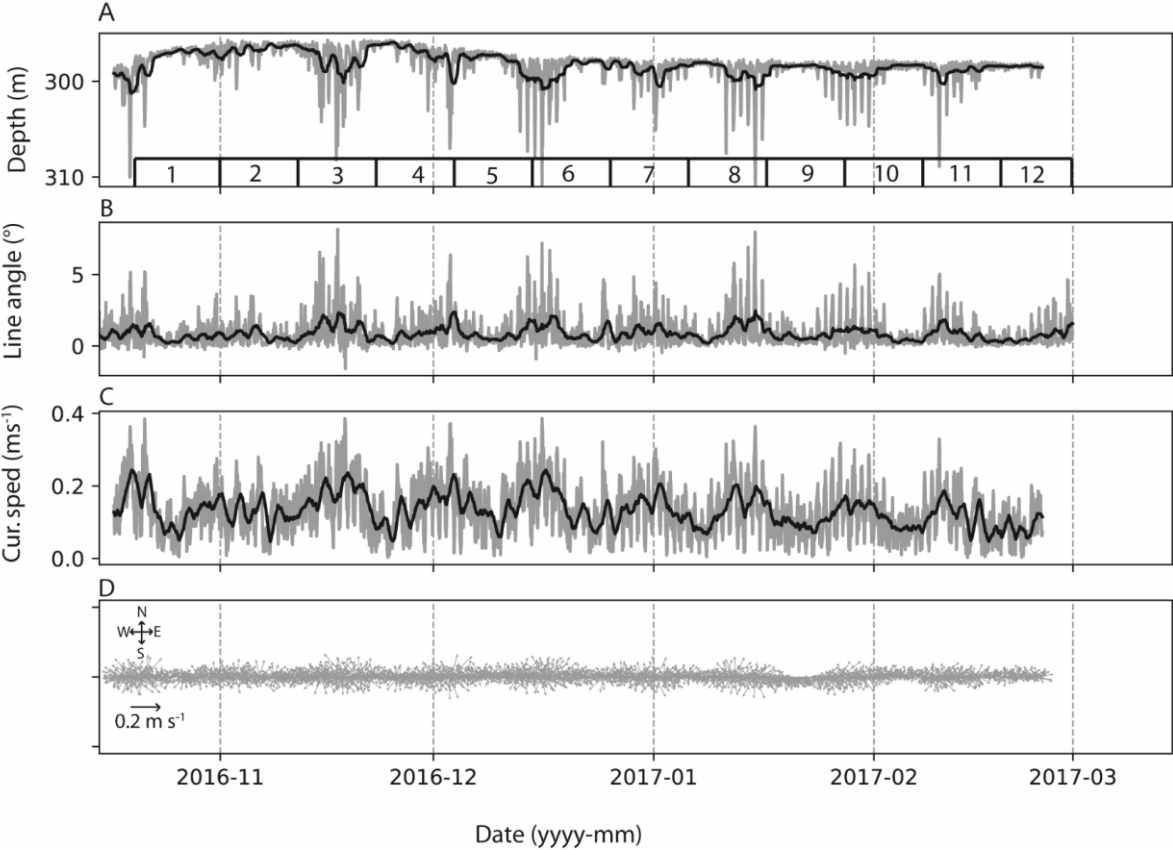


Figure 3

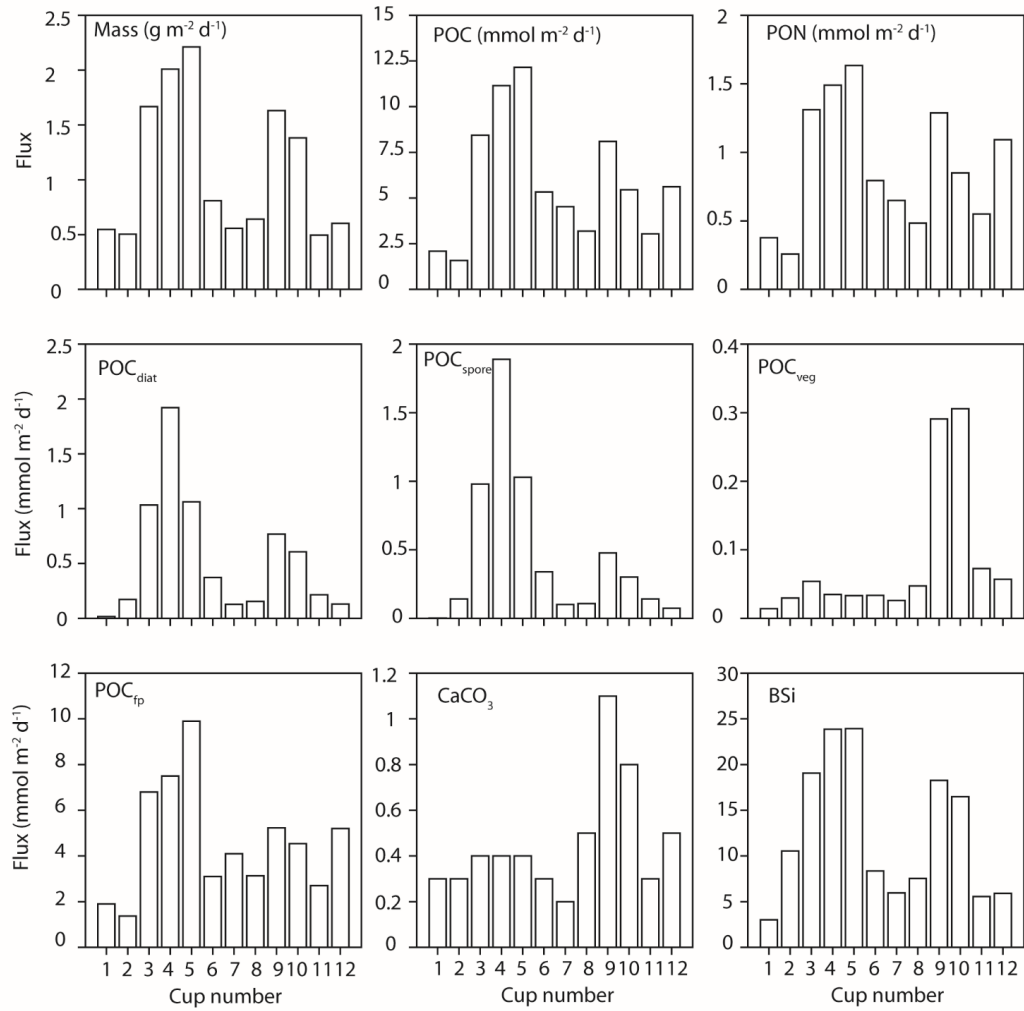


Figure 4

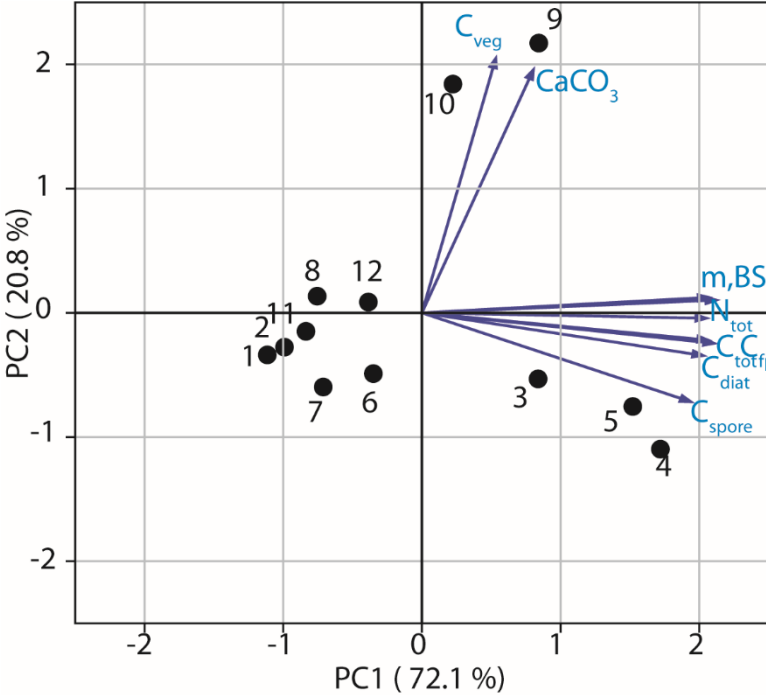


Figure 5

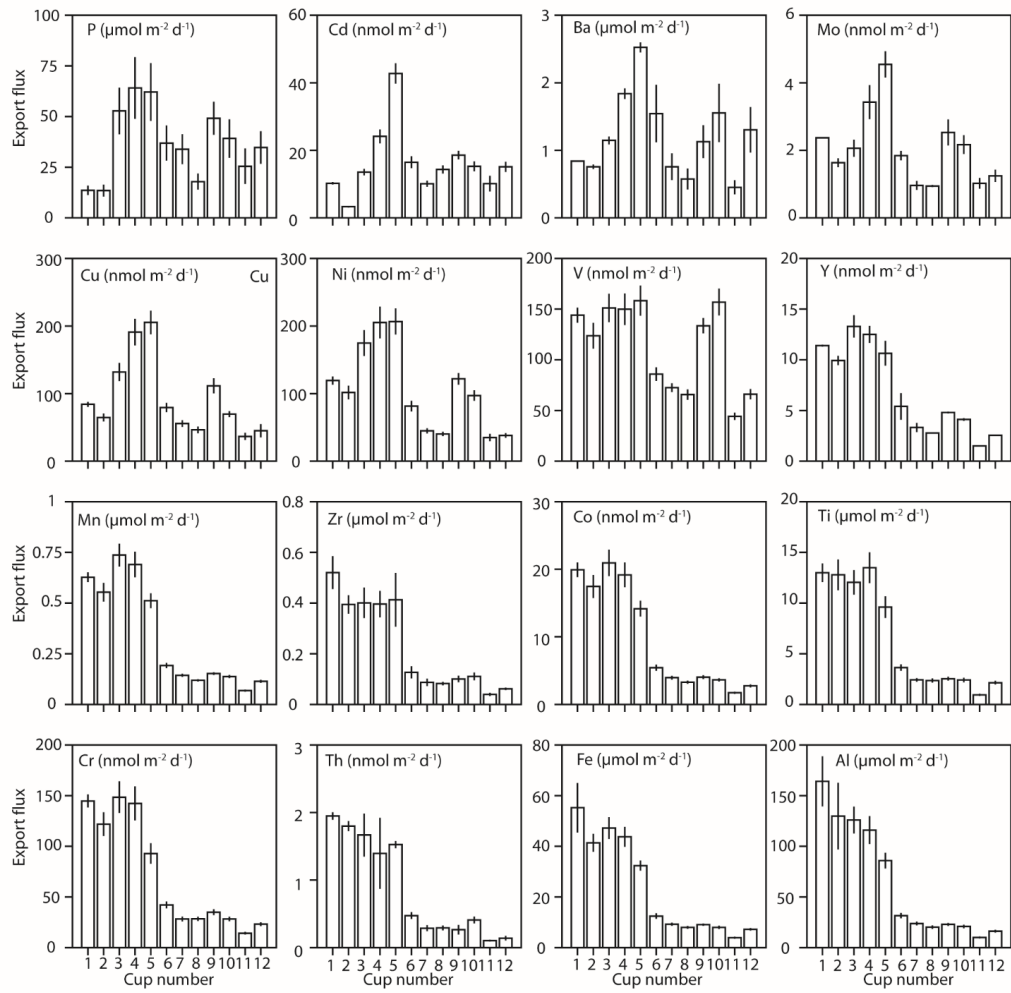


Figure 6

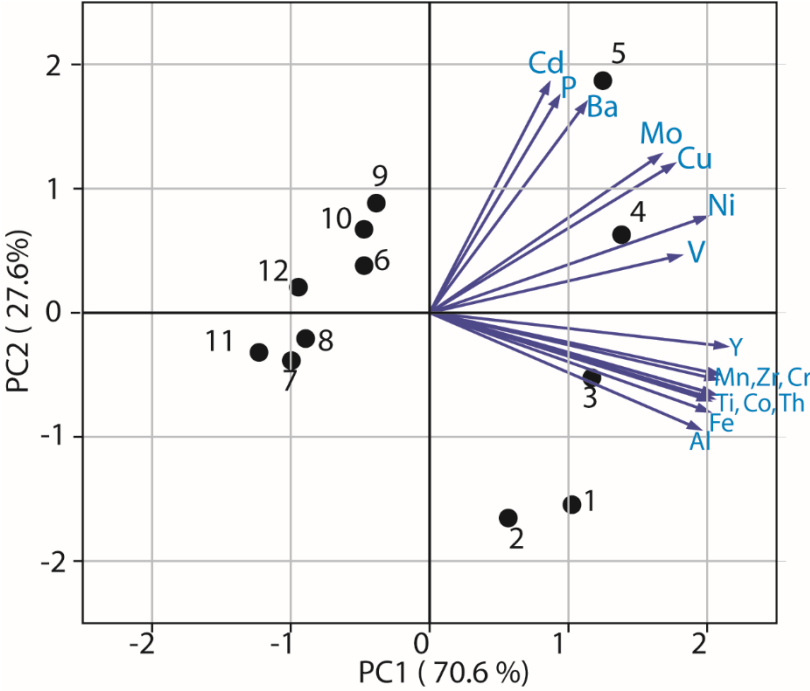


Figure 7

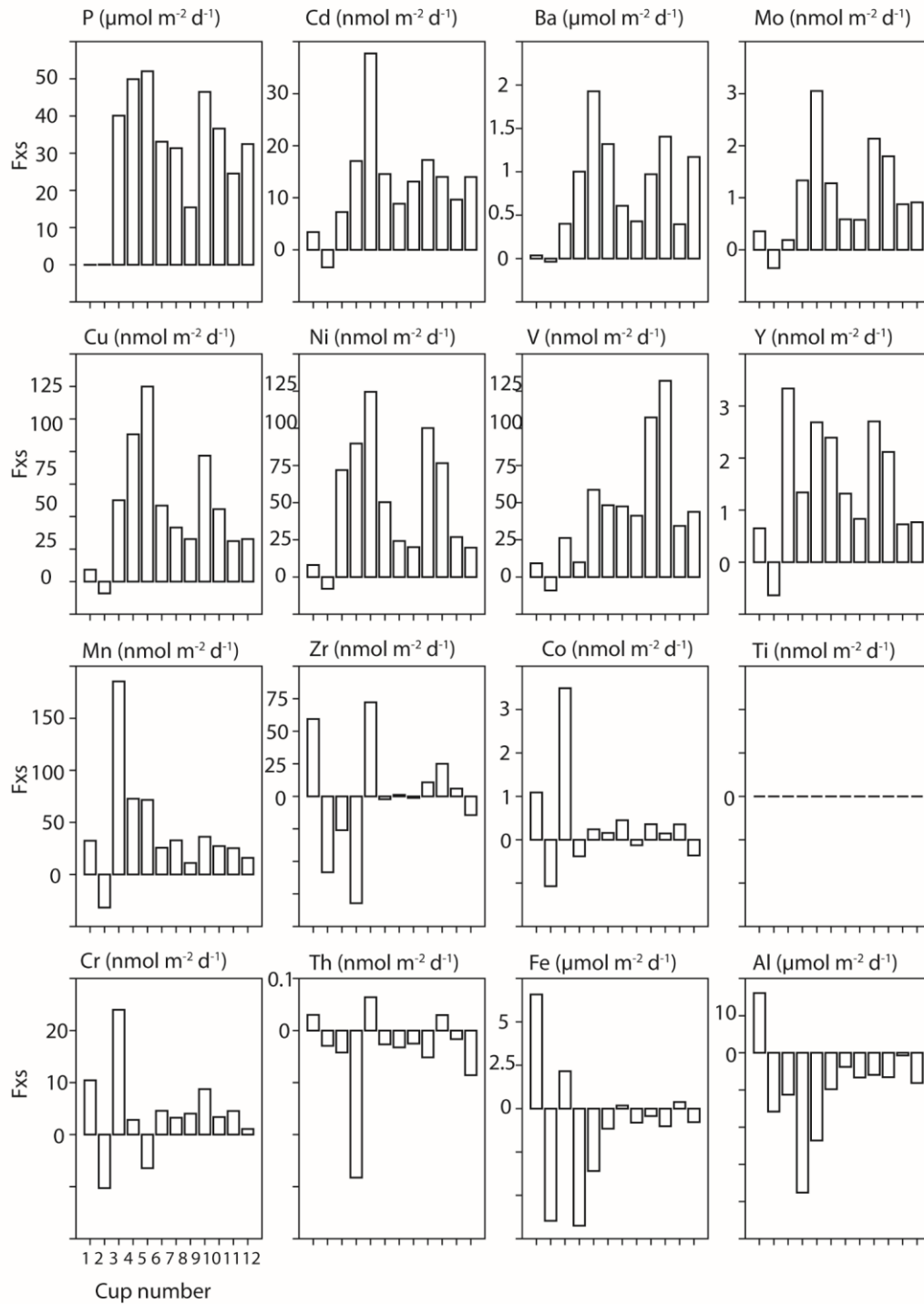


Figure 8

